OTC 20289

3D Inversion-Based Interpretation of Marine CSEM Data

J.J. Zach and M.A. Frenkel / EMGS

Abstract

The Marine Controlled-Source Electromagnetic (CSEM) method has been evolving into a geophysical imaging tool for increasingly complex geological settings, in which multiple resistive bodies can be resolved. An advanced subsurface imaging workflow for 3D CSEM surveys is presented, which reproduces the subsurface to within a spatial resolution determined frequencies included. The performance of our advanced processing workflow is demonstrated using a case study from the Gulf of Mexico, where a dense 3D grid was acquired over an area where high-quality seismic data, as well as well log control was given.

At the heart of our 3D workflow is an inversion methodology with approximate Hessian-based optimization and a fast finite-difference time-domain forward operator. The optimization matches the synthetic to the measured field within 100-200 iterations and is sufficiently robust in 3D to avoid expensive regularization schemes. The sensitivity of the gradient-based inversion to the starting model is addressed by investing considerable effort in building 1D inversion-based starting model. At the same time, 3D inversion algorithms for survey layouts including azimuthal data demand high quality data conditioning, for which we present a processing sequence from time-domain electromagnetic data acquired by seabed receivers to frequency domain data and weights for inversion.

Detection and delineation of reservoirs in the presence of salt is recognized as a major challenge to CSEM methods. In order to accurately interpret 3D data in such a complex environment, the true resistivity cube is built from a sequence of constrained inversion-based interpretation steps. Using a dataset acquired in 2008 in the Gulf of Mexico, we demonstrate the ability of our 3D-technology to resolve small (2km x 2km), low resistivity pay ($\Delta\rho<5\Omega$m) targets with in the vicinity (< 1km) of large salt bodies. In this case study, the 3D method converged within 1 week running on 150 parallel nodes.

Introduction

Marine controlled-source electromagnetic (CSEM) methods for hydrocarbon detection, which rely on a horizontal electric bipole emitting a predefined extremely low frequency spectrum, and the recorded electromagnetic fields by ocean bottom receivers, have been used in hydrocarbon exploration on a commercial scale since 2002 [1, 2]. The hydrocarbon detection mechanism is the relative enhancement of the transverse magnetic component of the received electromagnetic signal through a partial waveguide effect by resistors buried in the subsurface. These resistors can be either hydrocarbon deposits or other resistive bodies.

Advances in hardware and operations have resulted in a vast improvement in data quality, permitting the acquisition of well-defined and repeatable grids of seabed receivers with complex towing patterns including the acquisition of wide-azimuth data. Thus, marine CSEM has become a method for 3D imaging of complex geological settings, which is increasingly adopted by the industry, either as a standalone method or in conjunction with other geophysical probes, such as seismic [3] or MT [4]. Recent published case studies include [5-7].

To date, most solutions brought forward to solve the 3D marine CSEM problem rely on an iterative approach with repeated computation of the gradient of a misfit functional with respect to the discrete conductivity grid: $g = \partial \varepsilon / \partial \sigma$, where

the L2-norm is the most common choice for the data misfit: $\varepsilon = \sum\limits_{s,r,\omega,F} (\text{Weight})(\bar{x}_r \mid \bar{x}_s; \omega) \left| \Delta F_i (\bar{x}_r \mid \bar{x}_s; \omega) \right|^2$. Differences lie

mainly in the forward operators, the gridding of the forward and/or inversion grid and preconditioning approaches used in the optimization steps. Notable among the most recent contributions on inversion methodology are [4] on joint CSEM and MT inversion, as well as [8], which shows the importance of anisotropy in many surveys.

The 3D inversion methodology applied here is based on [9], where the gradient calculation is based on the first Born scattering assumption of the relationship between model- and field-perturbation. Due to electromagnetic reciprocity and the superposition principle, only two forward modeling steps per receiver are necessary to calculate the gradient from the difference field using a Green's function formulation [10]. To produce modeled data, a fast finite-difference time-domain solver was used [11]. The Born approach is similar to the approach used in [12], where the gradient was computed using an adjoint state method. In the optimization or update part of the iterative inversion, an approximation to the inverse Hessian matrix of second derivatives of the misfit with respect to the model parameters is obtained using a small number of past iterations in model- and gradient steps in an outer product- formulation [13]. Other inversion approaches proposed in recent years use mostly conjugate gradient loops, e.g., [14 - 16].

However, consistent inversion depends on error-proof conditioning and quality control of the data. A well-established workflow for inversion conditioning is presented here, which is based on [17]. Due to the sensitivity of a gradient-based inversion loop, the construction of a starting model which captures the main background trends of the subsurface is essential. Towards that, suitable individual receivers are inverted using a simulated annealing- based plane-layer inversion [17-18].

The resistivity of geologic salt deposits is found to be well in excess of hydrocarbon reservoirs, while the lateral extent is roughly comparable. Together with the marine CSEM frequency range of ~0.1-10 Hz impeding the differentiation of resistivities beyond ~10^2 Ωm, that has been rendering the detection of hydrocarbons in the presence of large concentrations of salt a major challenge. We were recently approached by Focus Exploration, LLC, a Gulf of Mexico (GoM) prospect generation company, to examine an area in the GoM with large concentrations of salt for possible hydrocarbon-bearing prospects in the vicinity of an existing and proven reservoir. In this study, we present 3D inversion of a receiver grid which includes the known reservoir as a calibration target.

Methodology 1: Data Conditioning

DATA PREPROCESSING WORKFLOW

Figure 1 shows the principal steps of the pre-processing workflow for inversion or other advanced processing in the frequency-domain, which was first completely introduced in [17]. The calibration of the data occurs in the time-domain and is dependent upon the specific receiver hardware used. Subsequently, they are converted as time-series data with a 50 Hz sampling rate into the processing data format, which is netCDF-based for both time- and frequency-domain data. While we expect a direct physical measurement of the seabed receiver orientation for at least some benchmark receivers in the near future, the receiver orientation is determined from the recorded electromagnetic field upon source-receiver passage. This limitation has been due to operational and cost reasons. The data for each receiver are ultimately rotated into a coordinate system in which "x" is defined as the source towline direction. The inline electric (crossline magnetic) field is then Ex (Hy), and Ey and Hx can only be larger than the noise floor if the symmetry is broken by either bathymetry or a resistive anomaly in the subsurface. The inline rotation, however, is not commutative with the estimate of the data uncertainty, or cumulative noise, which is essential for successful data inversion, and which occurs during demodulation. Two demodulation steps are therefore necessary in the overall workflow, where the rotation angles are determined during the first step, and are then used to rotate the data in the time domain.

The second demodulation step follows in the rotated coordinate system. The normalization of receiver data relative to the source in both magnitude and phase is conducted with the known source current and the measured time function measured by a reference receiver at the source. At the present state of the art, phase corrections are necessary for only 2-3% of receivers, in which the timing synchronization can be accurate to worse than 10 ms (~1 degree for 0.25 Hz). In those cases, the phase is corrected at close source-receiver passage for towlines which cross the receiver location, whereas any azimuthal lines are discarded.
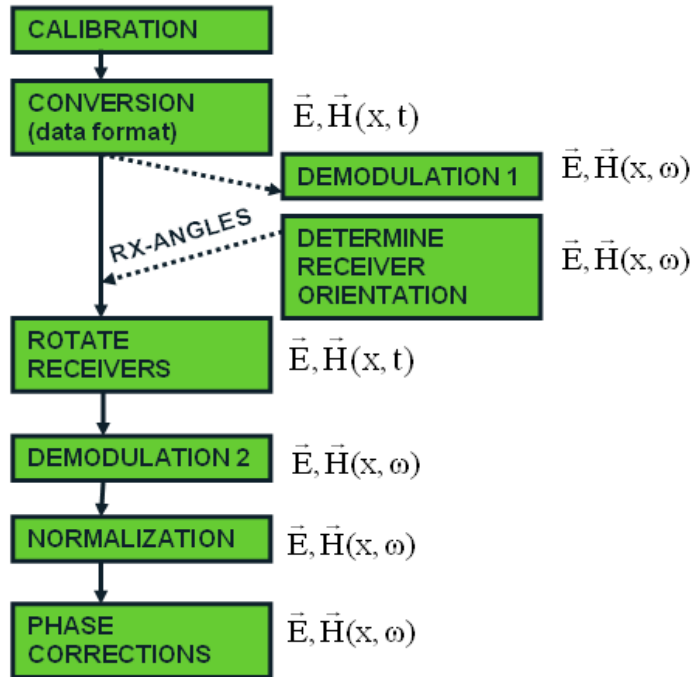
Fig. 1 - Main steps in preprocessing workflow for frequency-domain 3D inversion of marine CSEM data.

SOURCE WAVEFORM AND SPECTRUM

Traditionally, a square pulse with a frequency of typically $f_0 \sim 0.25 Hz$ is used in marine CSEM surveys, which naturally leads to a the occurrence of odd harmonic frequencies of the base frequency $(2n+1)f_0$, where the amplitude scales as $1/n$. More recently, customized source waveforms have become standard, in which a frequency spectrum can be tuned to accommodate a specific depth of investigation or resolution [19]. Figure 2 shows the source waveforms for both a recent survey example from the GoM (the bottom row), as well as a standard 0.25 Hz-square pulse (the top row), both in the time- and frequency domain. Both cases show a finite source switching time of 90 ms.
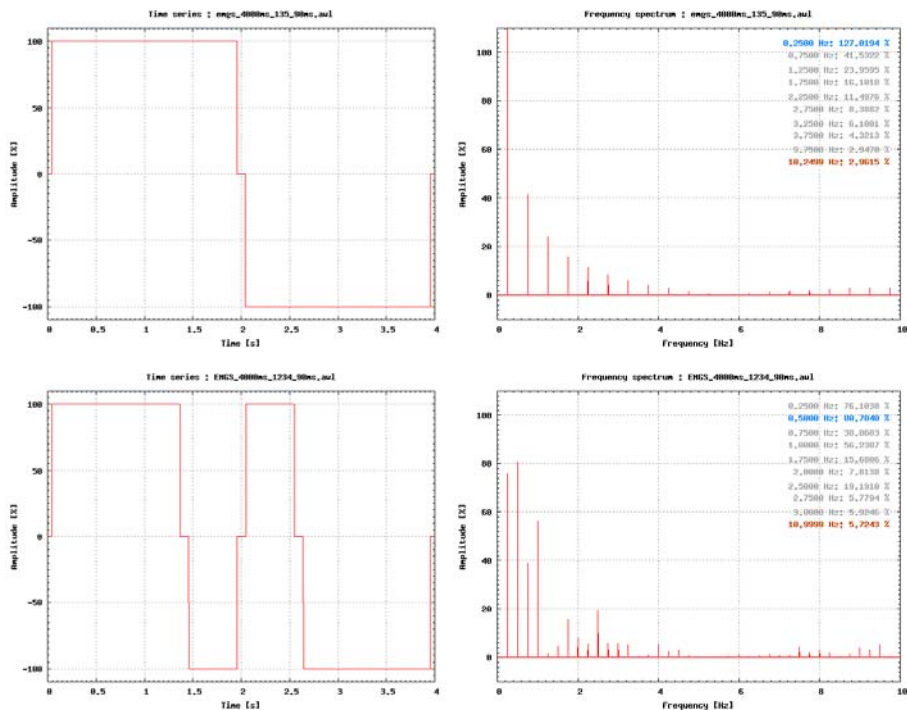

Fig. 2 - Source waveform in the time- (left) and frequency-domain (right; determined from source waveform using $J_{src}(\omega) = \int dt J_{src}(t) \exp(-i\omega t)$) for a traditional 0.25 Hz-square pulse (top), as well as a customized quadruple-waveform with four dominant frequencies: 0.25, 0.5, 0.75, and 1.0 Hz.

DATA DEMODULATION AND NOISE EXTRACTION

A short-time Fourier transform is applied to the seabed receiver data. The integration window of about 25-50 periods is thereby equivalent to the time it takes for the source to cross approximately one source length with a typical towing speed of 1-2 knots. The noise associated with a given frequency mode f_i, which will be essential in determining the data weights in the inversion, is approximated by the magnitude ratio between f_i and a given frequency range $\Delta f_{int} < \frac{1}{2}$ $(f_{i+1}-f_i)$ in the spectral neighborhood of the mode (see Fig. 3). The resulting signal and average noise amplitudes for three modes are plotted in the center panel of Fig. 2. The dominant noise source in the example shown in Fig. 3, acquired in deep-water in the Gulf of Mexico, is the electronics with relatively flat frequency dependence in the range from ~0.1-10 Hz. In shallower water and/or latitudes far away from the equator, magnetotelluric noise has been observed to dominate at lower frequencies. However, different noise characteristics for individual sensors including their electronics, as well as the superposition with natural noise sources (mainly ocean currents), renders the averaging procedure illustrated in Fig. 3 a highly nonlinear operation, hence, the rotation of the data in the time-domain.
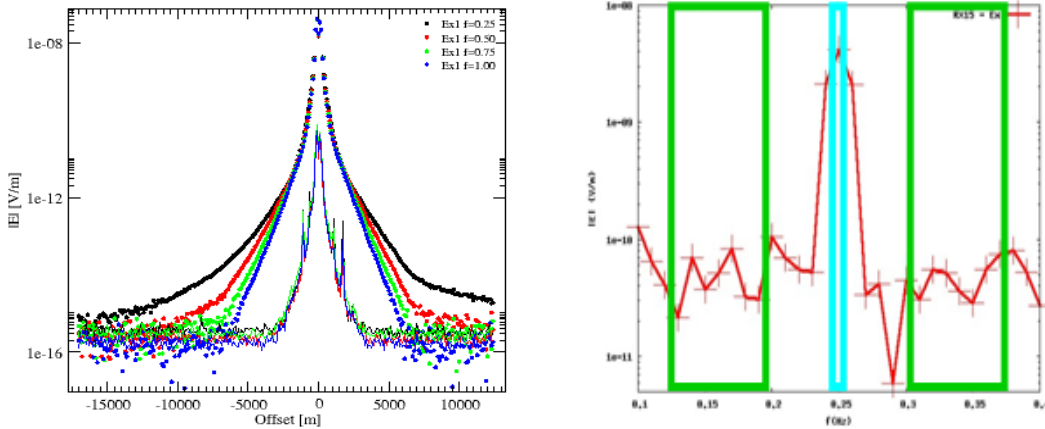
Fig. 3 - Left: magnitude-versus-offset curve for a receiver in a recent deep-water GoM acquisition. The scatter curves show the inline (i.e., in the same direction of the source bipole) component of the electric magnitude for the source frequency modes shown in Fig. 2, and the line curves the noise estimate illustrated in the right panel (see also text). Right: receiver spectrum at offset +4 km around the base frequency of a recent deep-water example (blue box). The green boxes define the frequency averaging windows to find a noise approximation.

RECEIVER ROTATION

Accurate determination of the receiver orientation presently necessitates towing the source over each receiver at least once, upon which the orientation relative to the source towline is found using the data-driven approach described in [20]. An example for the receiver rotation angle versus offset is shown in Fig. 4. Generally, the accuracy achieved is around 5 degrees, however, the uncertainty can be higher for tilted bathymetries, particularly with the tilt perpendicular to the towline.
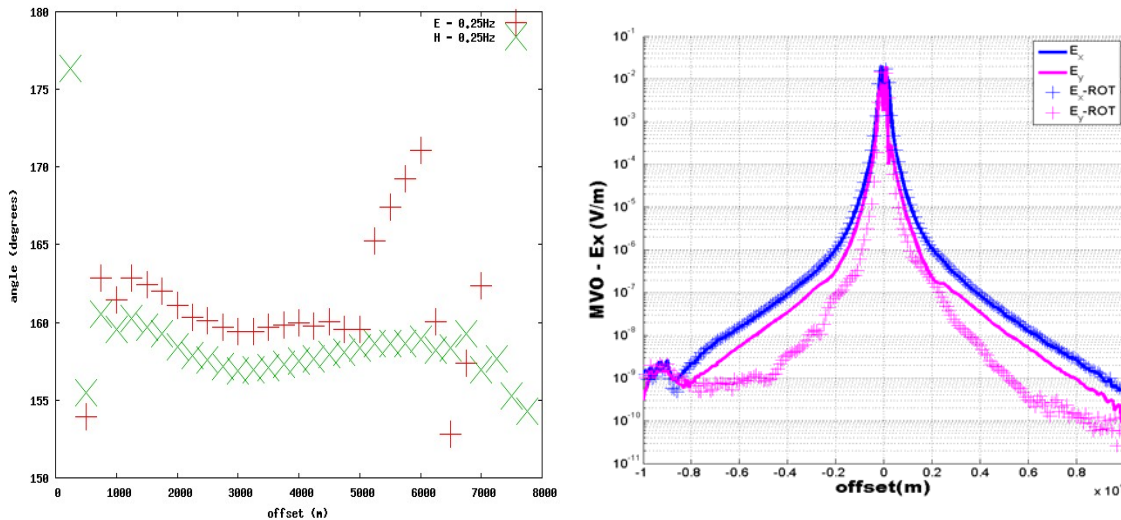
Fig. 4 - Inline rotation of receivers. Left: orientation versus offset from electric (red curve) and magnetic field (green curve) at 0.25 Hz (base frequency in a square input pulse) for an example receiver. Right: comparison of the horizontal electric field before (Ex, Ey) and after (Ex-ROT, Ey-ROT) coordinate transformation into towline coordinates.

AZIMUTHAL DATA

The 3D inversion scheme presented here relies on matching both magnitude and phase. Hence, a prerequisite for full 3D inversion including azimuthal data is accurate timing synchronization between source and receiver, which is illustrated in Fig. 5. With the present state of the art, this is given for 98% of all receivers.
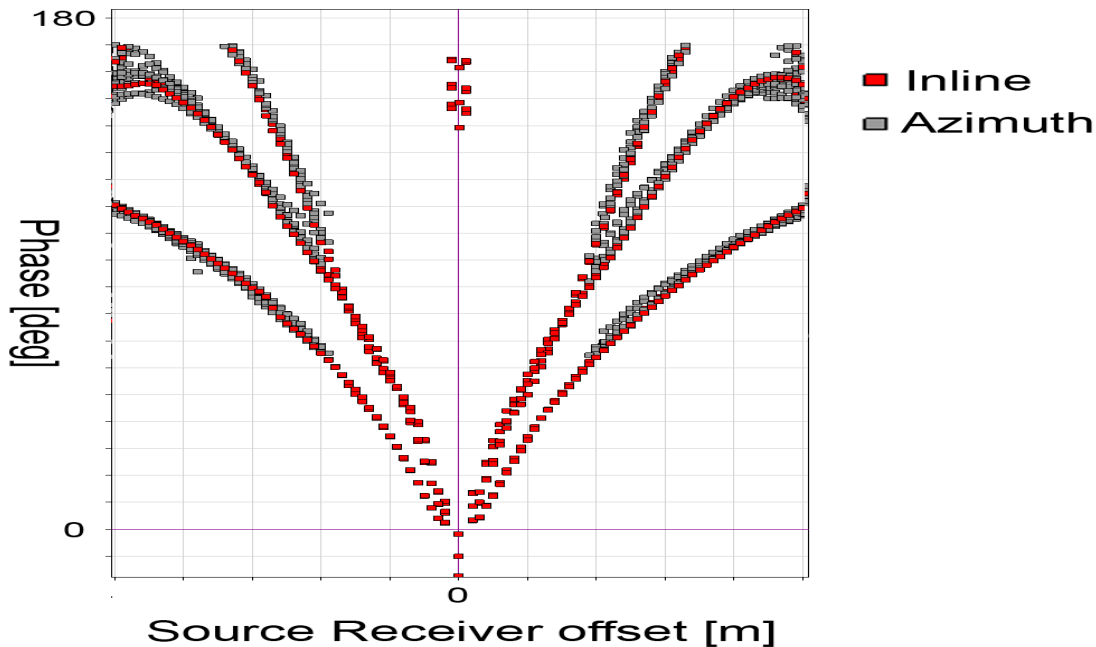

Fig. 5 - Selected receivers from a 3D-survey from the Norwegian Sea (2008): 1st and 3rd harmonic frequency of both inline and azimuthal electric phase, showing consistent timing and, therefore, phase in azimuthal data.

Methodology 2: 3D Inversion

STARTING MODEL PREPARATION

During towing of the source, information on position and physical state parameters is continuously logged every 10 seconds. Among the position measurements from a suite of acoustic, echosounder and CPT- (conductivity, pressure, temperature) sensors, the measurements extracted for 3D inversion are:

- Source Position Information: horizontal position, source altitude above the seafloor, orientation, tilt and feathering.

- Model Parameters: mudline conductivity, and depth of water column from echosounder measurements, if either seismic information is unavailable or shallow water renders seismic seafloor profiles less accurate than echosounder profiles.

In the majority of 3D marine CSEM surveys conducted to date (and in the example shown in this study), accurate 3D seismic data was available for the position of all receiver drops, and was used to build a discretized conductivity grid, in which only the seafloor conductivity was used in starting model preparation. Since CSEM towlines generally cover 20-30 km, which is greater than seismic data coverage, the grid was extrapolated using proprietary procedures.

Gradient-based inversion schemes such as the 3D inversion approach presented here are sensitive to its starting model, both from the standpoint of achieving a unique solution, as well as computational resources used to achieve data convergence. This is chiefly due to the large parameter space on the order of 10^7 unknowns, if we assume an inversion grid of ($\Delta x \times \Delta y \times \Delta z$) ~ (200 m x 200 m x 50 m). Hence, numerically less complex inversion schemes are used to produce a starting model which approximates large-scale conductivity trends of the real model. The standard approach is to execute plane-layer inversion of individual receivers with a robust simulated-annealing inversion scheme [17, 18] and to interpolate a layered resistivity model from the resulting conductivity-depth-profiles. As a pre-stage to full 3D inversion, plane-layer inversions of several to, if necessary, all receivers are run to identify general trends and to determine a starting model. Each receiver thus included is inverted for receiver data for 2-3 frequencies and for the Ex- and Hy-fields simultaneously. The depth is discretized using a stretched grid with 30-100 bins from mudline, and using an exponential cooling scheme, convergence is typically reached after 10^4 iterations (a few hours on a single processor). In order to avoid sharp resistivity contrasts which might create artifacts in the inversion, smoothness constraints are enforced in the individual plane-layer inversions; this implies that only receivers which do not exhibit resistive anomalies can be included in building the starting model.

In practice, this excludes receivers, for which the data cannot be explained to within the predefined measurement accuracy for a predefined smoothness constraint in a stretched, plane-layer resistivity grid. The starting model such produced is essentially a model of the vertical resistivity. Therefore, if well logs of substantial depth coverage are available, they can only be included in building starting models, if at least a good estimate of the electrical anisotropy is available.

WEIGHT GENERATION

The 3D inversion presented [9] relies on minimizing a misfit functional of the difference field between real and simulated data, which is based on the L2-norm:

$$\varepsilon_{data} = \sum_{s,r,\omega,F} W^F(\vec{x}_r \mid \vec{x}_s; \vec{J}, \omega) |\Delta F_i(\vec{x}_r \mid \vec{x}_s; \vec{J}, \omega)|^2 = \sum_{r,\omega,F} \varepsilon^F(\vec{x}_r; \vec{J}, \omega).$$

The data weights W^F are determined in a binary weighting scheme, where they are set to zero if the noise estimate at the frequency and offset in question is insufficiently suppressed:

$$W^F = \frac{1}{|\vec{F}|^2}, |F| > (SNR_{thr})\sigma_F$$

$$W^F = 0, |F| < (SNR_{thr})\sigma_F.$$

Otherwise, the data weight estimate is based on the magnitude squared of the measured field only, to avoid any a priori offset bias in the inversion. Figure 6 shows a data example from deep-water Gulf of Mexico which illustrates the determination of the data weights and the L2-kernel which contributes to the misfit function to be minimized. As signal to noise- (SNR-) cutoff, a standard threshold of 26dB was used. The synthetic data are produced using the finite-difference time-domain code described in [11].
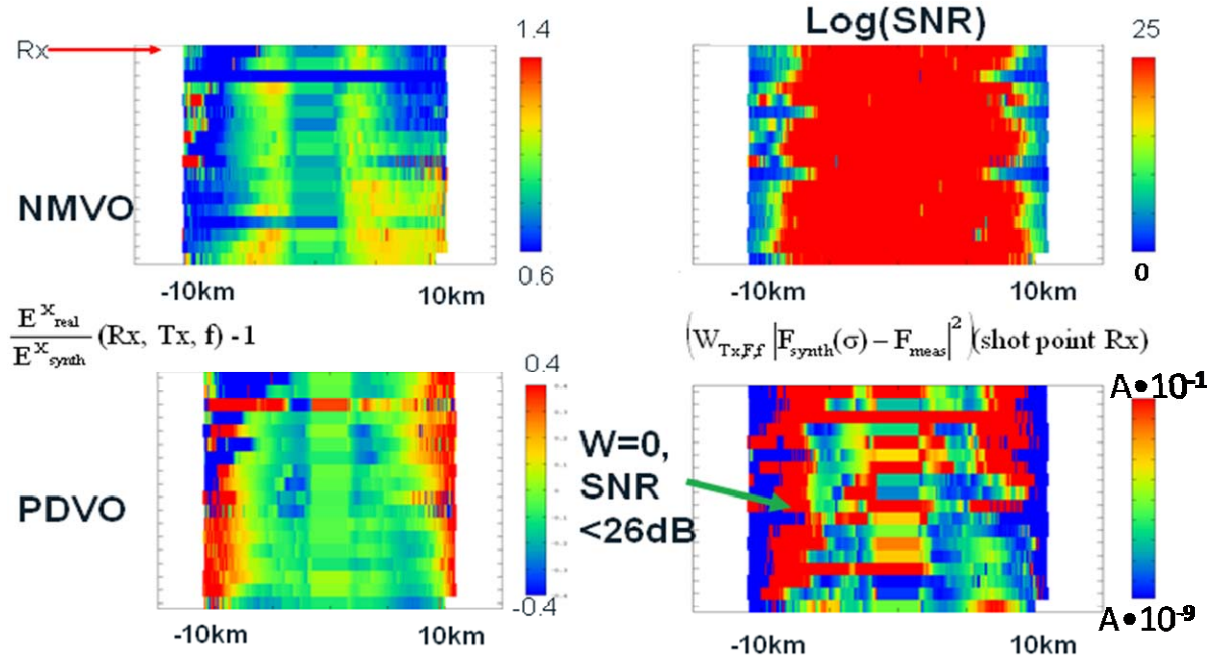

Fig. 6 - **Convergence summary plots for iteration zero (starting model) in the inversion of a recent deep-water data example: upper/lower left: relative misfit in magnitude/phase versus offset in percent/radians. Upper right: approximate signal-to-noise ratio. Lower right: L2-kernel, accounting for offset ranges which are weighted down due to too low SNR, as well as offsets which an inverse scheme will act upon. The square of the inverse measured data was used to determine the weights: W=1/|F$_{meas}$|^2. The data misfit indicates a conductive CSEM anomaly.**

3D INVERSION METHODOLOGY

The 3D case study presented here was inverted following [9], using a quasi-Newton method, where the inverse Hessian is approximated by an outer product formulation of the vectors of an integer number of past iterations' update steps and gradient changes (following [13]). The forward problem is solved with the finite-difference time-domain solver described

in [11], and the gradient is calculated at each iteration using a Green's function approach [10], based on the assumption of the first Born-approximation applied to the difference field between synthetic and real data.

The 3D inversion proceeds in the iterative loop shown in Fig. 7, where the input consists of the starting model and the conditioned data and weights. Due to better noise suppression compared to magnetic data, only the electric field was used in the inversion, whereas inline and azimuthal data from next-neighboring lines were included. A generic survey design for 3D acquisition is shown in Fig. 8. Data convergence to within measurement accuracy is achieved within 80-200 iterations (1 week on 150 parallel nodes). A dominant potential source of error, particularly for azimuthal data, is the data-driven determination of the receiver rotation angles. However, while towing the source over each receiver was still necessary to accurately determine its orientation, azimuthal data could be recovered which is accurate to within 5% in magnitude and 5 degrees in phase.

3D INVERSION – OPTIMIZATION

Each of the iterations in the update module in Fig. 7 consists of a quasi-Newton update step to minimize an approximation to the misfit functional in the neighborhood of the present location in configuration space:

$$\varepsilon(\sigma) \approx \varepsilon(\sigma_0) + \nabla\varepsilon(\sigma_0)(\sigma - \sigma_0) + \frac{1}{2}(\sigma - \sigma_0)^{\mathrm{T}}\nabla^2\varepsilon(\sigma_0)(\sigma - \sigma_0)$$

$$\sigma - \sigma_0 = -\upsilon_0\left[\nabla^2\varepsilon(\sigma_0)\right]^{-1}\nabla\varepsilon(\sigma_0)$$

Here, υ_0 is a scalar < 1 and the gradient of the misfit functional with respect to a model change is written as $g = \left[\nabla\varepsilon\right] = 0$, and the inverse Hessian matrix $\left[\nabla^2\varepsilon\right]^{-1}$ is approximated using an outer product formulation of the vectors of an integer number m of past iterations' update steps and gradient changes [9, 13].
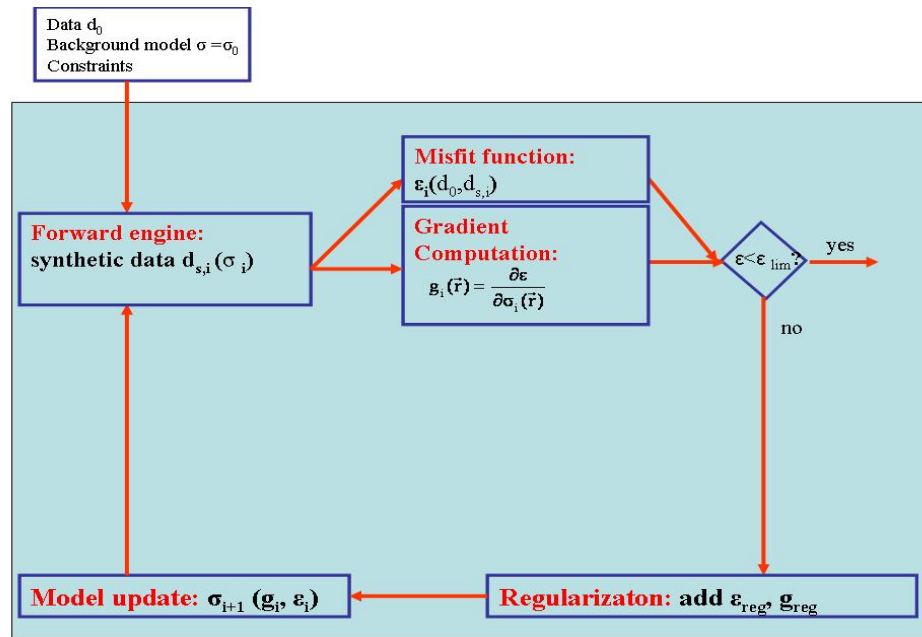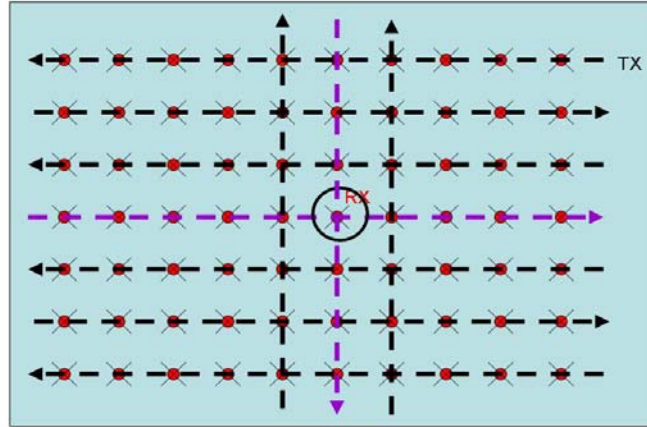

Fig. 7 - Iterative loop for gradient-based inversion, consisting of a forward Maxwell solver, misfit function and gradient calculation, a regularization step and an optimization step.

Fig. 8 - Generic survey design for 3D acquisition with dashed source towlines and red receiver positions. The line spacing is at most 1.5km, and for a given receiver RX, we refer to the lines crossing its position as "inline", and to all other lines as "azimuthal" lines.

3D INVERSION – FORWARD MODELING, GRADIENT CALCULATION

The forward modeling step is based on the finite-difference time-domain code described in [11]. The gradient calculation [10] is based on the first Born approximation, which assumes a linear relationship between the field perturbation δF^{synth} due to a model perturbation $\delta\sigma(x)$:

$$\delta F_i^{synth}(\vec{x}_r|\vec{x}_s;\vec{J},\omega) \approx \sum_{\vec{x}} G_{in}^{FJ}(\vec{x}_r|\vec{x};\omega)G_{nk}^{EJ}(\vec{x}|\vec{x}_s;\omega)J_k(\vec{x}_s;\omega)\delta\sigma(\vec{x}),$$

which, for an L2 misfit functional, leads to:

$$\frac{\delta\varepsilon^F(\vec{x}_r,\omega)}{\delta\sigma(\vec{x})} \approx \pm G_{ni}^{ES}(\vec{x}|\vec{x}_r;\omega)\sum_s G_{nk}^{EJ}(\vec{x}|\vec{x}_s;\omega)W^F(\vec{x}_r|\vec{x}_s;\omega) \bullet \Delta F_i^*(\vec{x}_r|\vec{x}_s;\vec{J},\omega)J_k(\vec{x}_s;\omega) + C.C.$$

The Green's functions $G_{ni}^{ES}(\vec{x}|\vec{x}_r;\omega)$ define the modeled field in the n-direction due to a unit source S in the direction i (electric source J or magnetic source K) at x_r. Since the computational domain is reciprocal, with receivers comprising the modeled sources, the + (-) signs are used for an electric (magnetic) source. The sum over all source points s is equivalent to a distributed source with the amplitude given as the weighted difference field; due to the electromagnetic superposition principle, this sum can be calculated for all (reciprocal) receiver locations in one forward modeling step. Hence, only two forward modeling steps are needed to obtain the partial gradient for each receiver and measured field component.

3D INVERSION – PRECONDITIONING AND REGULARIZATION

In addition to the data misfit, the model itself can be subjected to constraints such as smoothness, proximity to a preferred model, resistive boundaries or limits in the parameter space. The extent to which this should be applied depends on the prior knowledge about the model. However, it has been observed that in 3D inversion, even unconstrained inversion leads, in most cases, to meaningful, given sensible choices for data weights and starting models. Further, various strategies can be applied to modify the gradient with a preconditioner to improve the convergence rate of the inversion (see [9]).

Gulf of Mexico Case Study

CHALLENGES

We present a case study from the Gulf of Mexico (GoM), in a block where detailed 3D seismic data was available. We were approached by the client to probe the area for additional hydrocarbons, which might make an existing, and proven, hydrocarbon discovery commercial. The water depth is around 1000 m, with the proven hydrocarbon deposits consisting of three stacked layers between 1800-2000 m TVD. The task was to identify the hydrocarbon potential of various seismic leads and to discriminate between fizz gas and commercial pay. Generally, the example presented is considered one of the most challenging successful marine CSEM surveys conducted to date, for the following reasons:

- From well control, we know that the proven reservoir is a ~2 km x 2 km- resistor with low-resistivity pay (4-5 Ωm), which is, in itself, recognized as a challenging EM-target. The overburden consists of shales with complex resistivity

boundaries, and resistivities of up to 2-2.5 Ωm. The situation will be similar for the other leads, which are anticipated in the same geologic formation.

- Extensive salt deposits with a complex distribution are found stacked underneath the proven reservoir and the leads, with depth separation of 500-1500 m.
- Some of the source towlines crossed a pipeline, the location of which had been unknown prior to the survey. Due to secondary source effects, which cannot be compensated in processing due to a conductivity contrast of around seven orders of magnitude and unknown design details, this led to a swath of data within ~1km of the pipeline to be discarded. Besides the loss in coverage, this necessitated lengthy manual processing, since the pipeline was not mapped.

PROCESSING AND INVERSION

A starting model was built using the available seafloor bathymetry information from the seismic surveys and the measured conductivity. Concerning constructing a starting model, Fig. 2 shows results from three plane-layer inversions, in which data convergence to within the measurement accuracy was achieved with smoothness constraint of 0.5 Ωm/bin in most of the model. In the complex 3D geology, the plane layer inversion results are only quantitatively reliable for short offsets and shallow depths. These shallow layers confirm shale resistivities between 1.5-3 Ωm. Deeper than 600-800 m below mudline, a conductive layer is recovered, which is associated with brine-saturated sandstone, as confirmed by well control. At depths greater than 1.3-2 km below mudline, the resistivity gradually increases, signifying the appearance of salt.
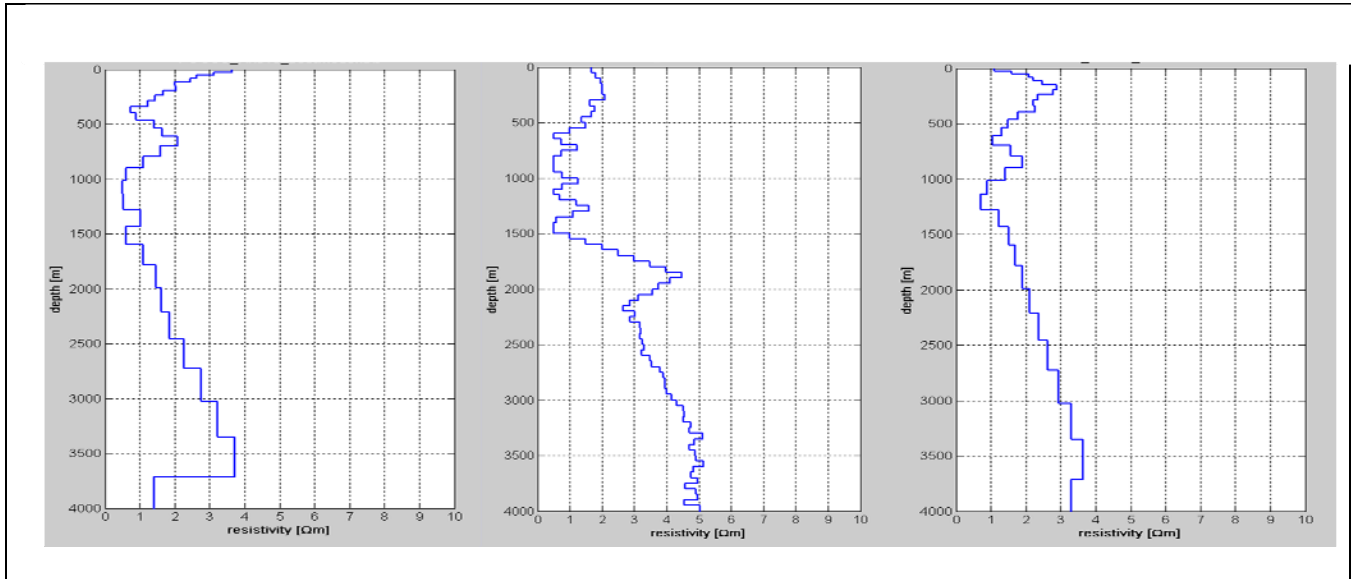
Fig. 9 - Plane-layer inversion of the receiver indicated as a black (left), purple (center) and white (right) circle in Fig. 12.

Results of full 3D inversion for two different starting models will be shown:

1) Using the average resistivity obtained for the first 500 m, a 2 Ωm-halfspace model was first used to avoid any bias.
2) From interpreting the plane-layer inversions, the initial resistivity linearly decreases from 2 Ωm to 1 Ωm from mudline to 500 m depth, below which a 1 Ωm-halfspace is used.

The full electric field of the four dominant frequency modes between 0.25-1.0 Hz is inverted in the examples shown next. In all cases, inline data and azimuthal data from neighboring lines were included in the inversion.

RESULTS

The results from inversion of the full dataset for starting model 1, projected on one grid line (line in top panel of Fig. 11), is shown in Fig. 10, confirming the overall geology known from 3D-seismics and well-control. A representative data QC plot, showing overall convergence to within the accuracy of the marine CSEM method (5 degrees in phase, 5% in magnitude), despite of the non-optimal starting model, is shown in the lower panels of Fig. 10.
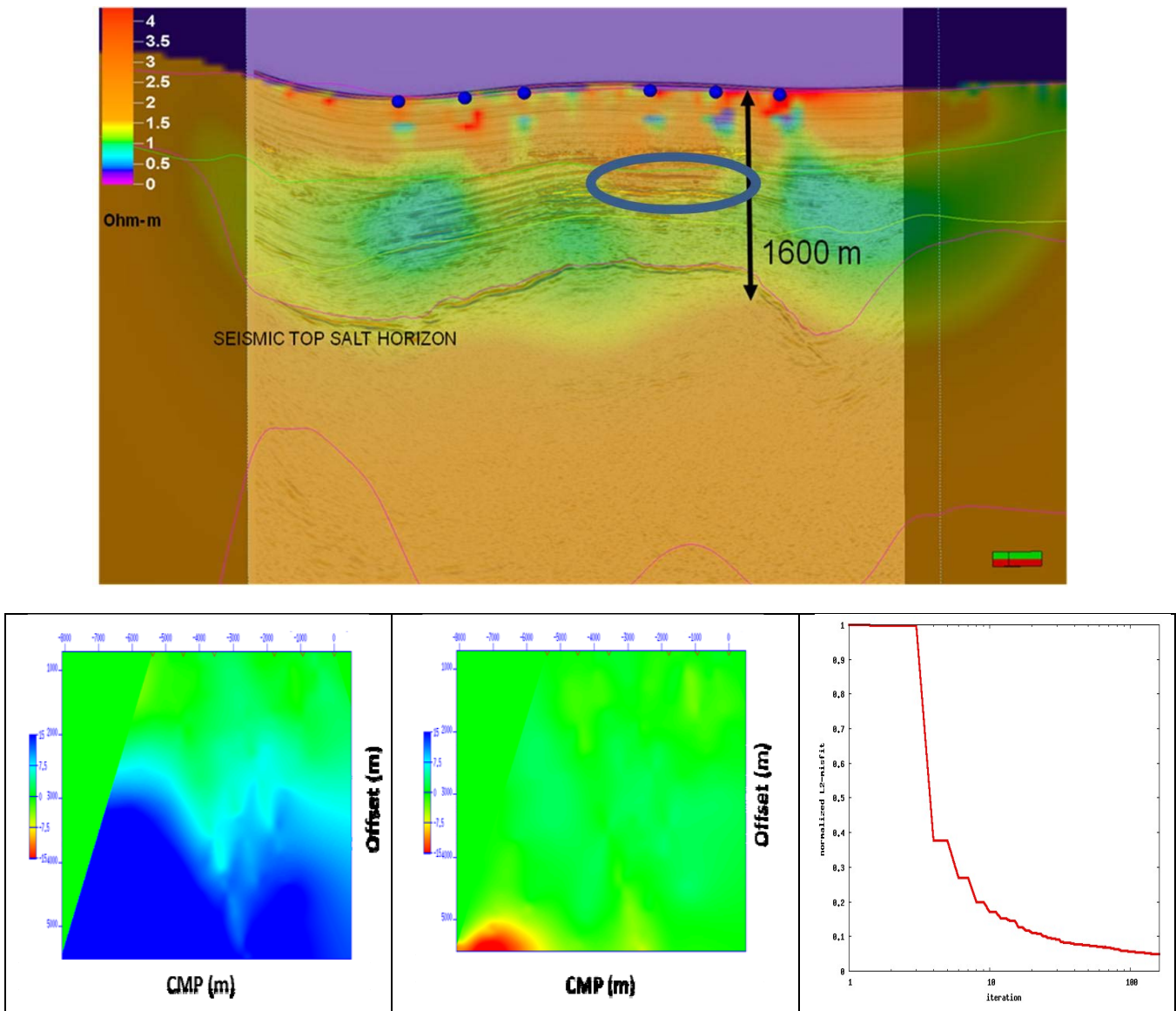
Fig. 10 - Top: Projection of the resistivity cube from the final unbiased 3D inversion onto the dashed line on Fig. 11, overlaid with a 3D seimic-image, along with the interpreted seismic top-salt horizon. The top-salt horizon is recovered to within 50-150 m, whereas most of the deviation occurs below the proven hydrocarbon reservoir. Features in the subsurface known from well control and extensive seismic data, including the brine-saturated sandstone and the shale in shallow regions, are also recovered. However, the hydrocarbon reservoir (blue oval) is only imaged with good quality with subsequent analysis. Left (center) panel: data misfit for initial (final) model in the phase for the f=0.5 Hz-mode, showing convergence to within the measurement accuracy (representative for magnitude and phase for all frequencies). Right panel: evolution of the misfit functional versus iteration number.

While the hydrocarbon reservoir is recovered from the unbiased inversion, seismic data and geologic knowledge of the shale overburden are needed for identification. The result is less ambiguous, however, for the complex starting model 2, which correctly recovers the depth of the stacked pay zones to within the resolution of the CSEM method (~10% of the burial depth). A detailed image of the resulting final resistivity cube is shown in Fig. 11, overlaid with seismic images and the well log. While the stacked anomalies were too closely packed to be separated by the method, the inversion clearly shows a maximum at the effective peak resistivity, which corresponds to the effective transverse resistance ($R_t=\Delta\rho \bullet \Delta z$) of the combined stacked resistors. In this context, it has to be stressed that the inversion was unconstrained, apart from choosing a starting model which captured most of the background features of the real model.

The lateral delineation of the proven target (purple prospect) is clearly shown by the different slices along example towlines. Figure 12 shows a depth section with constant depth below mudline for the prospect level of the proven reservoir, which has led the client to reconsider the extent of the proven reserves from the original estimates. Figure 13 shows the same depth slices for various seismic horizons in the model, which show the complex resistivity structure in the shales (1, 2) going into the reservoir underneath the shales (3, 4), and a level which marks the lower edge of the bulk resistivity found (5). The client was mainly interested in anomalies at similar depths below mudline in the "Southern" (orientation falsified) end of the

area, which is for that reason not shown in great detail in Fig. 13. Figure 14, finally, shows a representative inversion data fit for the final inversion result with starting model 2, similar to the lower panels of Fig. 10.
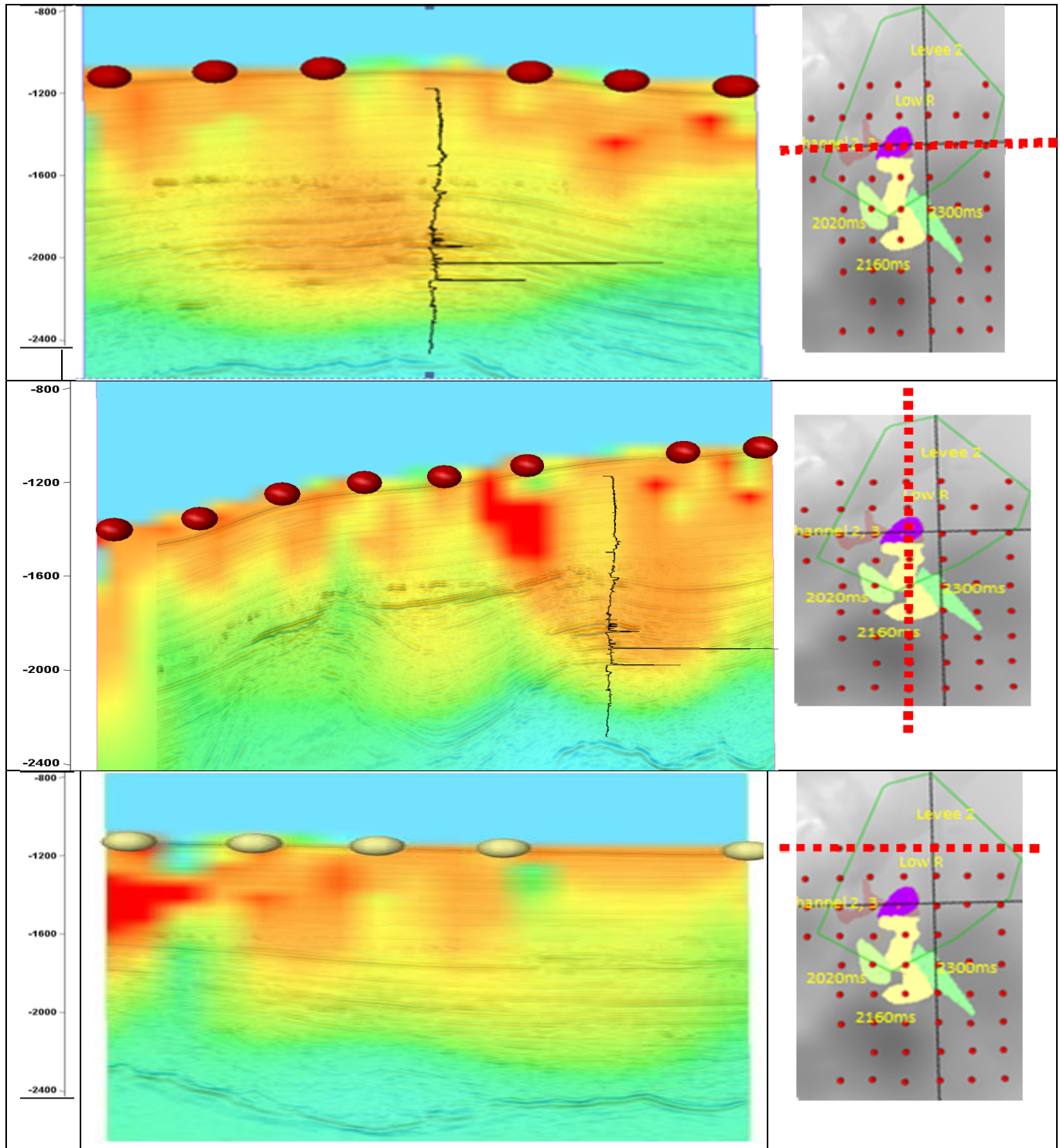

Fig. 11 – Projections of the resistivity cube from the final 3D inversion with complex starting model onto the towlines marked in the right panels, overlaid with a 3D seimic-image. Also shown is the well log, which marks the proven hydrocarbon reservoir, which is recovered to within 10 % of the burial depth. Prior geologic knowledge of the area indicates that the shallow features in the shales above the proven reservoir are real, and not due to receiver imprints. The latter, however, is responsible for some of the features closer than 200-300 m to the receivers.
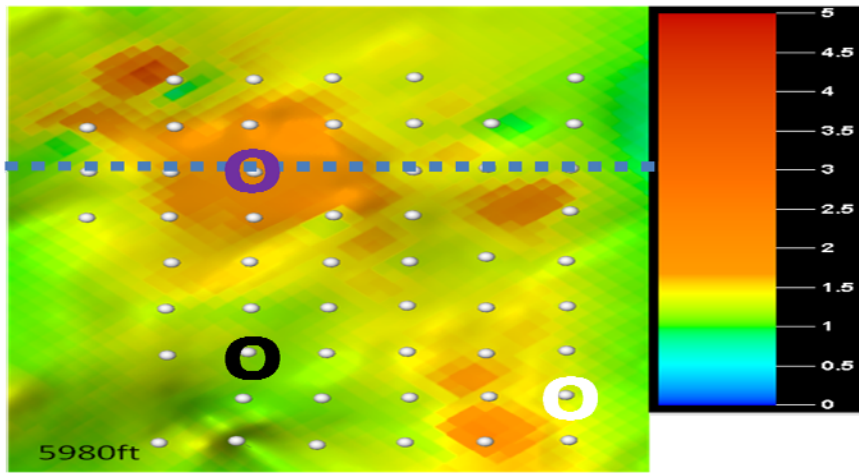
Fig. 12 - Resistivity map at constant depth below mudline from full 3D inversion at a certain reservoir depth slice. The three circles mark the reference receivers used in determining the 1D profiles shown in Fig. 9.
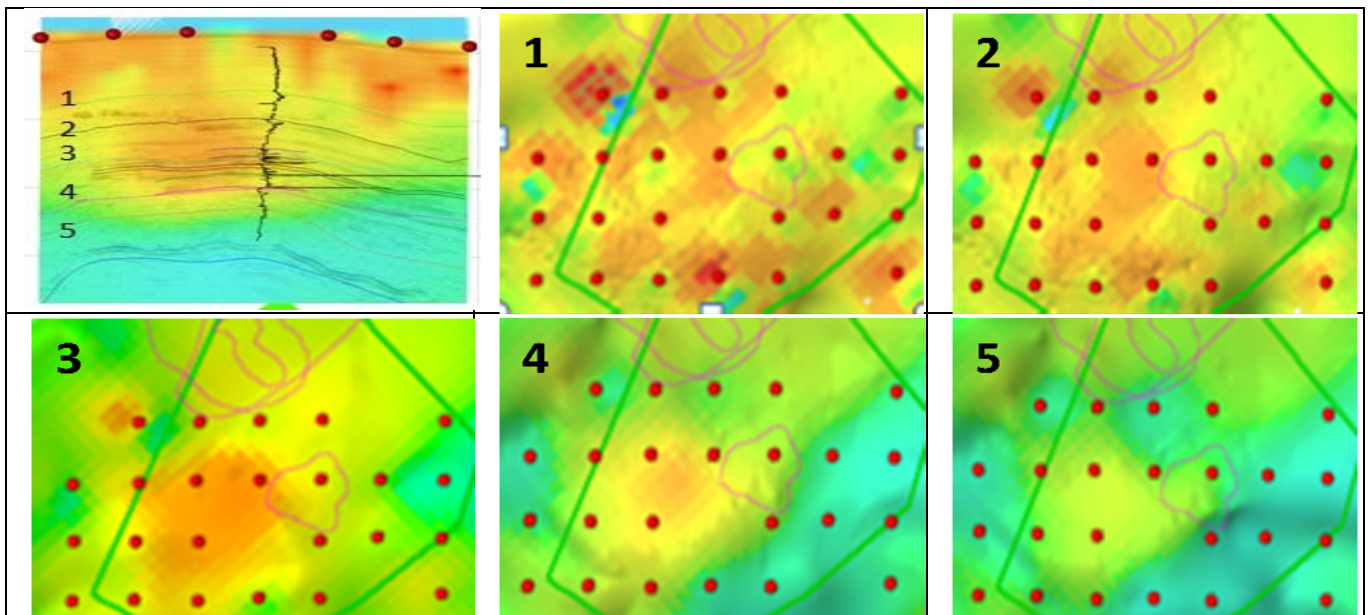

Fig. 13 - 3D resistivity cross-section overalyed with the resistivity well log (top left, in the same plane as the top panel in Fig. 11), and horizontal slices at various representative seismic horizons also shown in the 3D resistivity image in Fig. 12.
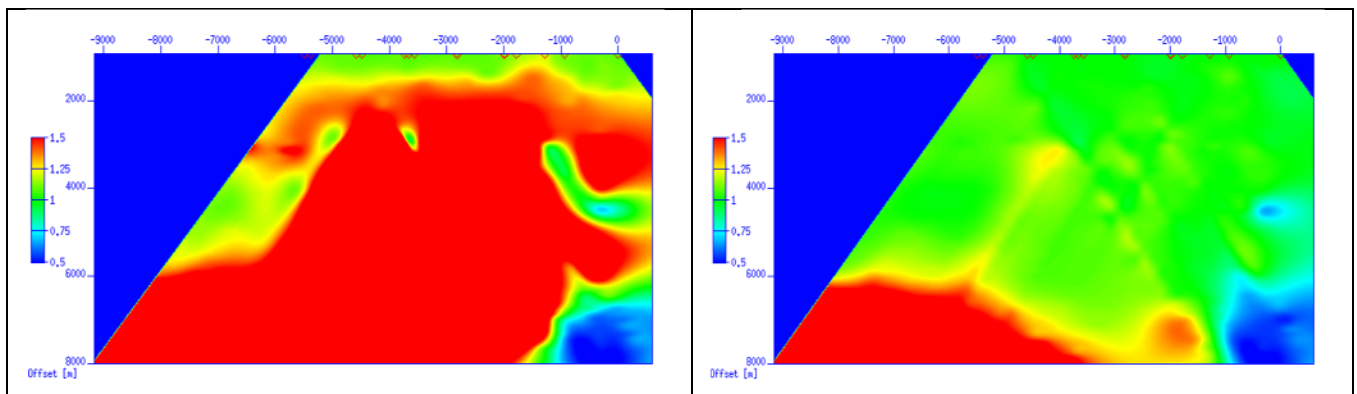

Fig. 14 – Representative 3D inversion QC data misfit plot: left (right): data misfit for initial (final) model in the magnitude for the f=0.5 Hz-mode, showing convergence to within the measurement accuracy for offset ranges corresponding to the reservoir horizons.

Conclusions

We have presented an inversion-based 3D interpretation technology, which is able to image complex geologies including multiple resistive targets underneath grids of seabed receivers. The entire workflow from data conditioning to 3D-inversion is robust and streamlined, and allows for inclusion of wide-azimuth data. Our experience with inverting real surveys is that after less than 300 iterations, the match between observed and synthetic data is at best 5% in amplitude and 5 degrees in phase, which is within the accuracy of our acquired survey data. With synthetic data and misfit gradients for several frequencies being computed in one forward modeling, the inversion manages one field component and receiver per node, which translates into, at most, a few hundred computational nodes as cluster peak-load. For typical 3D-surveys, the code manages 30-40 iterations per day on a state-of-the-art cluster, which has one node per receiver available at any time.

Using 3D acquisition grids and our gradient-based 3D inversion, we have achieved a practical convergency of the method in this state-of-the-art case study within 1 week on 150 parallel nodes. We have also demonstrated the applicability of marine CSEM methods to image a known reservoirs in the close vicinity (<1 km in vertical distance) of complex salt structures. Thereby, we have responded to the client's request, which was to seek similar reservoirs to the known pay in the same prospect. This implies the applicability of our CSEM technology to "salt provinces" such as the Gulf of Mexico.

Acknowledgements

References

[1] Eidesmo, T., Ellingsrud, S., MacGregor, L.M., Constable, S., Sinha, M.C., Johansen, S., Kong, F.N. and Westerdahl, H. (2002) Sea Bed Logging (SBL), a new method for remote and direct identification of hydrocarbon filled layers in deepwater areas. *First Break*, 26, 83-88.
[2] Johansen, S., Brauti, K., Fanavoll, S., Amundsen, H., Wicklund, T.A., Danielsen, J., Gabrielsen, P., Lorentz, L., Frenkel, M., Dubois, B., Christensen, O., Elshaug K., and Karlsen S. (2008) How EM survey analysis validates current technology, processing and interpretation methodology. *First Break*, 20, 144-152.
[3] Norman, T., Alnes, H., Christensen, O., Zach, J.J., Eiken, O., Tjåland, E. (2008) Planning Time-lapse CSEM-surveys for Joint Seismic-EM Monitoring of Geological Carbon Dioxide Injection. *EAGE Budapest 2008* CO2 Geological Storage Workshop.
[4] Commer, M., Newman, G.A. (2008) Optimal conductivity reconstruction using three-dimensional joint and model-based inversion for controlled-source and magnetotelluric data, *SEG 2008 Expanded Abstracts*, Las Vegas, NV, USA.
[5] Carrazone, J.J., Dickens, T.A., Green, K.E., Jing, C., Wahrmund, L.A., Willen, D.E., Commer, M., Newman, G.A. (2008) Inversion study of a large marine CSEM survey. *SEG 2008 Expanded Abstracts*, Las Vegas, NV, USA.
[6] Price, A., Turpin, P., Erbetta, M., Watts, D., Cairns, G. (2008) 1D, 2D and 3D modeling and inversion of 3D CSEM data offshore West Africa. *SEG 2008 Expanded Abstracts*, Las Vegas, NV, USA.
[7] Plessix, R.-E., van der Sman, P. (2008) Regularized and blocky controlled source electromagnetic inversion. *PIERS 2008*, Cambridge.
[8] Jing, C., Green, K.E., Willen, D.E. (2008) CSEM inversion: Impact of anisotropy, data coverage, and initial models. *SEG 2008 Expanded Abstracts*, Las Vegas, NV, USA.
[9] Zach, J.J., Bjørke, A.K., Støren, T., Maaø, F. (2008) 3D inversion of marine CSEM data using a fast finite-difference time-domain forward code and approximate Hessian-based optimization. *SEG 2008 Expanded Abstracts*, Las Vegas, NV, USA.
[10] Støren, T., Zach, J.J., Maaø, F. (2008) Gradient calculations for 3D inversion of CSEM data using a fast finite-difference time-domain modelling code, *EAGE 2008 Expanded Abstracts*, Rome, Italy.
[11] Maaø, F. A. (2007) Fast finite-difference time-domain modeling of marine-subsurface electromagnetic problems. *Geophysics*, **72**(2), A19-A23.
[12] Plessix, R.-E., van der Sman, P. (2007) 3D CSEM modeling and inversion in complex geological settings. *SEG 2007 Expanded Abstracts*, San Antonio, TX, USA.
[13] Byrd, R.H., Lu, P., Nocedal, J. (1995) A Limited Memory Algorithm for Bound Constrained Optimization. *SIAM Journal on Scientific and Statistical Computing*, 16, 5, 1190-1208.
[14] Commer, M., Newman, G.A., Carazzone, J.J., Dickens, T.A., Green, K.A., Wahrmund, L.A., Willen, D.E., Shiu, J. (2008) Massively parallel electrical-conductivity imaging of hydrocarbons using the IBM Blue Gene/L supercomputer, *IBM Journal of Research and Development*, 52, 93-103.
[15] Mackie, R.L., Watts, M.D. (2007) Joint 3D Inversion of marine CSEM and MT data. *SEG 2007 Expanded Abstracts*, San Antonio.
[16] Gribenko, A., Zhdanov, M. (2007) Rigorous 3D inversion of marine CSEM data based on the integral equation method. *Geophysics*, 72, WA73-WA84.
[17] Zach, J.J., Roth, F., Yuan, H. (2008) Data preprocessing and starting model preparation for 3D inversion of marine CSEM surveys. *EAGE 2008 Expanded Abstracts*, Rome, Italy.
[18] Roth, F., Zach, J.J. (2007) Inversion of marine CSEM data using up-down wavefield separation and simulated annealing. *SEG 2007 Expanded Abstracts*, San Antonio, TX, USA.
[19] Mittet, R., Schaug-Pettersen, T. (2007) Shaping optimal transmitter waveforms for marine CSEM surveys. *SEG 2007 Expanded Abstracts*, San Antonio, TX, USA.
[20] Mittet, R., Aakervik, O.M., Jensen, H.R., Ellingsrud, S., Stovas, A. (2007) On the orientation and absolute phase of marine CSEM receivers. *Geophysics* 72, F145-F155.